HHS Public Access

Author manuscript

Biochim Biophys Acta. Author manuscript; available in PMC 2017 November 01.

Published in final edited form as:

Biochim Biophys Acta. 2016 November ; 1860(11 Pt A): 2335–2344. doi:10.1016/j.bbagen.2016.06.023.

First comprehensive structural and biophysical analysis of MAPK13 inhibitors targeting DFG-in and DFG-out binding modes

Zeynep Yurtsever[1,2,3], **Dhara A. Patel**[1], **Daniel L. Kober**[1,4], **Alvin Su**[1], **Chantel A. Miller**[1], **Arthur G. Romero**[1], **Michael J. Holtzman**[1,5], and **Tom J. Brett**[1,3,5,6]

[1]Division of Pulmonary and Critical Care Medicine, Department of Medicine, Washington University School of Medicine, St. Louis, Missouri 63110

[2]Biochemistry Program, Washington University School of Medicine, St. Louis, Missouri 63110

[3]Center for the Investigation of Membrane Excitability Diseases, Washington University School of Medicine, St. Louis, Missouri 63110

[4]Microbiology Program, Washington University School of Medicine, St. Louis, Missouri 63110

[5]Department of Cell Biology and Physiology, Washington University School of Medicine, St. Louis, Missouri 63110

[6]Department of Biochemistry and Molecular Biophysics, Washington University School of Medicine, St. Louis, Missouri 63110

Abstract

BACKGROUND—P38 MAP kinases are centrally involved in mediating extracellular signaling in various diseases. While much attention has previously been focused on the ubiquitously expressed family member MAPK14 (p38α), recent studies indicate that family members such as MAPK13 (p38δ) display a more selective cellular and tissue expression and might therefore represent a specific kinase to target in certain diseases.

METHODS—To facilitate the design of potent and specific inhibitors, we present here the structural, biophysical, and functional characterization of two new MAPK13-inhibitor complexes, as well as the first comprehensive structural, biophysical, and functional analysis of MAPK13 complexes with four different inhibitor compounds of greatly varying potency.

RESULTS—These inhibitors display IC_{50} values either in the nanomolar range or micromolar range (>800-fold range). The nanomolar inhibitors exhibit much longer ligand-enzyme complex half-lives compared to the micromolar inhibitors as measured by biolayer interferometry. Crystal

Address correspondence to: Tom J. Brett, PhD., Campus Box 8052, 660 S. Euclid, St. Louis, MO 63110. Phone: (314) 747-0018; Fax: (314) 362-8987; (tbrett@wustl.edu).

Conflict of interest statement

The authors declare no competing financial interests.

PDB References: mitogen-activated protein kinase 13 (p38δ), complex with compound 58 5EKN; complex with compound 117, 5EKO.

structures of the MAPK13 inhibitor complexes reveal that the nanomolar inhibitors engage MAPK13 in the DFG- out binding mode, while the micromolar inhibitors are in the DFG-in mode. Detailed structural and computational docking analyses suggest that this difference in binding mode engagement is driven by conformational restraints imposed by the chemical structure of the inhibitors, and may be fortified by an additional hydrogen bond to MAPK13 in the nanomolar inhibitors.

CONCLUSIONS—These studies provide a structural basis for understanding the differences in potency exhibited by these inhibitors.

GENERAL SIGNIFICANCE—They also provide the groundwork for future studies to improve specificity, potency, pharmacodynamics, and pharmacokinetic properties.

Keywords

p38 kinase; structure-based drug design; chronic inflammatory lung disease; kinase inhibitor; inhibitor half-lives; differential scanning fluorimetry

1. Introduction

The mitogen activated protein kinase (MAPK) p38α (MAPK14) is the founding and most studied member of the p38 MAPK family. MAPK14 is ubiquitously expressed and centrally involved in pro- inflammatory signaling; it has thus been the focus of numerous drug-development projects for several diseases involving chronic inflammation, including rheumatoid arthritis and inflammatory bowel disease [1-4]. Recent breakthroughs in structure-based drug design have resulted in highly specific and potent inhibitors to MAPK14 [5-7], but there are remaining concerns as to the practicality of targeting this enzyme, since knockout of this gene in mice results in embryonic lethality [8-10], and efforts to develop MAPK14 inhibitors have ended in failed drug trials, usually due to toxicity [11]. In contrast to MAPK14, other members of the p38 MAPK family display restricted tissue and cellular expression, and therefore may represent viable targets for specific diseases. Along these lines, MAPK11 (p38β) is highly similar to MAPK14 (75% sequence identity), whereas MAPK12 (p38γ) and MAPK13 (p38δ) are more sequence diverse (62% and 61% identical to MAPK14, respectively). Also, the MAPK12/MAPK13 double knockout mouse displays no detrimental phenotypes, only reduced innate inflammatory responses induced by lipopolysaccharide (LPS) [12].

MAPK13 has recently emerged as a disease specific p38 MAPK drug target. Compared to MAPK14, MAPK13 displays more tissue-specific expression patterns, and therefore contributes to more restricted functions [13, 14]. This restricted expression pattern suggests that this kinase may be targeted in specific biological pathways. For example, MAPK13 regulates insulin secretion and survival of pancreatic β-cells, and MAPK13-deficient mice are protected against insulin resistance induced by a high-fat diet and oxidative stress-mediated β-cell failure, suggesting a role in diabetes [15]. MAPK13 is also pivotal in neutrophil chemotaxis pathways, where it contributes to acute respiratory distress syndrome (ARDS) [16]. In addition, studies in knockout mice indicate that MAPK13 contributes to pathways activated in chronic inflammatory conditions [12], is centrally involved in

tumorogenesis in both colitis-associated colon cancer [17] and squamous cell carcinoma models [18], and is crucial for development of arthritis in certain models [19]. Finally, MAPK13 activation is required for IL-13-dependent airway mucus overproduction which is a characteristic feature of chronic inflammatory lung disease [20].

Given the role of MAPK13 in chronic lung disease (and possibly other diseases), we initiated the first structure-based drug project to develop inhibitors targeting MAPK13 [20]. This work also presented the first structures of MAPK13 complexes with inhibitors, and for any p38 MAPK family member other than MAPK14. As noted above, MAPK14 has been the subject of intense structure-based drug design efforts, and numerous structural and biophysical studies of MAPK14-inhibitor complexes have been reported (>170 structures in the PDB as of October 2015). Thus, much is known about the structural requirements for MAPK14 inhibition [21]. To develop a more complete understanding of the structural basis for activation of MAPK13, we developed methods to produce both unphosphorylated (inactive) and dually-phosphorylated (active) MAPK13 in quantities for structural and biophysical studies and used these proteins to study complexes with inhibitors for the purposes of targeting this kinase through structure-based drug design [20] [22]. Here we present a complete functional, biophysical, and structural characterization of two new MAPK13-inhibitor complexes, new biophysical data on two previously reported complexes, and the first comprehensive analysis of MAPK13 in complex with all four structurally characterized inhibitors, which display greatly varying potency. These studies reveal the structural basis for differences in potency for this set of inhibitors.

2. Materials and Methods

2.1. Materials

All inhibitors were synthesized at Washington University as described previously [20].

2.2. Expression constructs

Full-length human MAPK13 is 365 amino acids and contains several basic residues at the C-terminus. For crystallization, a slightly truncated MAPK13 construct (1-352) was designed and cloned into pET28a as a N-terminal 6-His-tagged construct using the *Nde*I and *Xho*I restriction endonuclease sites. A full-length human MAPK13 construct was prepared similarly to produce protein for enzyme inhibition and biophysical studies [20]. The construct was confirmed by sequencing. A pET28a construct of N-terminal-6-His-tagged lambda-phosphatase was a kind gift from Dima Klenchin (University of Wisconsin, Madison, WI).

2.3. Protein Expression and Purification

Constructs were transformed into Rosetta2 (DE3) *E. coli* (Stratagene) and colonies were grown on a plate with kanamycin selection (50 μg/mL). Cultures for protein expression were grown in Luria broth (LB) media using chloramphenicol (40 μg/mL) and kanamycin (50 μg/mL) selection. Both the MAPK13 crystallization construct (1-352) and full-length protein (1-365) were expressed and purified in a similar manner, as outlined here. Protein expression was induced at 30° C by addition of 0.5 mM isopropyl β-D-1-thiogalactopyranoside (IPTG)

and each 1L of media was enriched with 10 ml of saturated glucose solution during protein expression. Protein expression was carried out at 30° C for 4 hours.

Cell pellets were harvested by centrifugation and suspended in lysis buffer suitable for nickel- nitrilotriacetic acid (Ni-NTA) gravity chromatography (50 mM K_2HPO_4 pH 8.0, 300 mM NaCl, 10 mM imidazole, 10% glycerol, 10 mM 2-mercaptoethanol). Cells were lysed by addition of 0.5 mg/ml lysozyme and DNAse I followed by sonication. Clarified lysate was passed over Ni-NTA superflow resin (Qiagen), which was then washed with lysis buffer containing 20 mM imidazole and then proteins were eluted with 250 mM imidazole. The protein was further purified by gel filtration chromatography (Superdex 200) in a buffer consisting of 20 mM HEPES pH 7.5, 150 mM NaCl, 0.001% NaN_3, 5 mM dithiotreitol (DTT), and 10% glycerol. The protein eluted as a single peak correlating to a monomeric molecular weight [22]. This peak was harvested and then dephosphorylated *in vitro* by addition of lambda phosphatase (0.1 mg/ml) and 5 mM $MnCl_2$ at room temperature for 30 minutes, which was then quenched with 5 mM EDTA. This treatment was not very efficient and only increased the amount of dephosphorylated MAPK13 by about 10% [22]. Following dialysis against a buffer consisting of 20 mM Tris pH 8.0, 10 mM NaCl, 1 mM DTT, and 10% glycerol (buffer A) at 4° C overnight, the protein was then subjected to anion exchange chromatography using a MonoQ column (GE Lifesciences). Protein was injected onto the column using buffer A and then eluted off using a gradient from 0-60% of buffer B (20 mM Tris pH 8.0, 1 M NaCl, 1 mM DTT, and 10% glycerol) over 40 column volumes. This resulted in separation of unphosphorylated and phosphorylated MAPK13 [22]. The unphosphorylated MAPK13 peak was harvested and used for structural studies with inhibitors. Full-length MAPK13 for enzyme inhibition and biophysical assays was expressed and purified similarly.

2.4. Preparation of MAPK13-inhibitor co-crystals

Crystals of non-phosphorylated MAPK13 were obtained by mixing protein solution (at 10 mg/ml) with reservoir solution (50 mM ammonium tartrate, 18% PEG 3350) in a 4:1 (protein: reservoir) ratio, similar to as previously described by us [20]. Co-crystal complexes with inhibitor compounds 58 and 117 were prepared by soaking, similar to our previous work. Inhibitor compound stocks were prepared in DMSO at 100 mM and then added to crystal-containing drops at 1:10 volume, for a final inhibitor concentration of 10 mM in the drop. Crystals were allowed to soak for 10 minutes to 4 hours before cryoprotection in mother liquor supplemented with 25% ethylene glycol, followed by flash-freezing at −160° C in a chilled nitrogen stream.

2.5. Data collection, reduction and structure determination

X-ray diffraction data were collected at either the Advanced Photon Source (beamline 19-ID) or the Advanced Light Source (beamline 4.2.2). Data were indexed and processed with HKL2000 [23]. The phase problem was solved by isostructural replacement using the apo form of MAPK13 (PDB ID: 4YNO) [20] in an initial round of rigid body refinement. Compounds were clearly visible in $F_O - F_C$ difference maps following rigid body refinement (see Fig. 3). Model rebuilding and compound fitting to electron density maps was performed manually using Coot [24] and refinement was carried out in PHENIX [25]. Structural

analysis of MAPK13-inhibitor contacts was performed in LigPlot+ [26]. All molecular graphics figures were produced using PyMOL [27]. All crystallographic software were obtained and maintained by the SBGrid distribution [28]. Diffraction images were deposited with the Structural Biology Data Grid [29]. Data collection and refinement statistics are summarized in Table 1.

2.6. Differential Scanning Fluorimetry

Melting temperature of MAPK13 and MAPK14 was measured in the presence of inhibitors (58, 61, 117, 124) using a Protein Thermal Shift Dye Kit (Life Technologies, CA) according to manufacturer's specifications. This assay used both the unphosphorylated and the phosphorylated forms of MAPK13 and unphosphorylated MAPK14 at a final concentration of 0.15 mg/ml in the reaction mixture. A titration experiment was carried out first to demonstrate specificity and establish dynamic range. Based on this, single point experiments were carried out on all kinases using a final inhibitor concentration of 25 μM. Each condition was replicated five times. The experiment was carried out on a 7500 Fast Real-Time PCR System (Life Technologies, CA) using the melt curve template. The initial incubation step at 25 °C was modified to be 30 minutes to ensure complex formation between the inhibitors and the proteins. Data were analyzed using Protein Thermal Shift Software v1.1 (Life Technologies). Additional statistical analysis was carried out in Prism v5.0c. Results are summarized in Figure 6 and Table 3 and presented as mean ± S.E.M. Replicate experiments were carried out using three different protein preps on different days to obtain mean ± S.E.M.

2.7. MAPK13 Inhibition Assay

Compounds were assayed for inhibition of MAPK13 kinase activity using an immobilized metal affinity polarization (IMAP) as previously described [20]. Briefly, the assay contained activated (phosphorylated) MAPK13, a FITC-labeled substrate, and the test compound. Experiments were carried out at concentrations in the linear phase of the rate kinetics. Assay reactions contained 0-100 μM test compound, 5-35 nM (EC_{80}) activated MAPK13, 3 μM ($K_{m,app}$) ATP, and 100 nM FITC- labeled EGFR peptide substrate (FITC-KRELVERLTPSGEAPNQALLR-NH_2). The IC_{50} values for each compound were determined from the compound concentration versus fluorescence polarization (mP) plot using nonlinear curve fitting.

2.8. Inhibitor binding kinetics measured by biolayer interferometry

Kinetics of MAPK13 binding to small molecules was assessed using bio-layer interferometry with an Octet (ForteBio, Menlo Park, CA) as described previously [20]. MAPK13 was randomly biotinylated *in vitro* using EZ-link NHS-PEG4-Biotin (Thermo Scientific) at a 1:2 molar ratio (protein: reagent). Super-streptavidin-coated biosensors from ForteBio were used to capture biotinylated MAPK13 onto the surface of the sensor. After reaching baseline, sensors were moved to association step for 300 s and then dissociation for 300 s. Curves were corrected by a double-referencing technique using both biotin- coated pins dipped into the experimental wells and a buffer-only reference. The binding buffer consisted of 20 mM HEPES pH 7.5, 150 mM NaCl, 0.005% Tween 20, and 5% DMSO.

MAPK13- inhibitor complex half-lives were calculated from dissociation constants determined from global kinetic analysis ($t_{1/2} = \ln 2/k_{dissociation}$).

2.9. Computational docking

In silico docking studies were carried out in GLIDE from the Schrodinger Suite [30, 31]. All inhibitors were treated as ligands and prepared from their SMILES strings using LigPrep without changing ionization states. Protein coordinates were imported from pdb files and processed using the Protein Preparation Wizard (PDB ID 4MP9 for MAPK13 DFG-out; 4MP5 for MAPK13 DFG-in; 1KV2 for DFG residues. Ligands were docked flexibly into the grid in Standard Precision (SP) mode. After the docking simulation was completed, the protein was overlapped with the coordinates from the co- crystal structures. RMSD between the docked coordinates and the crystal coordinates for the inhibitor was calculated using a command-line script, rmsd.py (available from http://www.schrodinger.com/scriptcenter/14). Results are summarized in Table 4.

3. Results and discussion

3.1. A series of inhibitors with greatly varied potencies for MAPK13

Here we report the steady-state, biophysical, and structural evaluation of a set of MAPK13 inhibitors. The inhibitor design was inspired by analyzing potent MAPK14-inhibitor complex structures, superposing on our unphosphorylated (apo) MAPK13 structure, and realizing smaller substituents in the ATP-binding pocket would be required for optimal binding [20]. Specifically, we focused on BIRB-796, which binds to MAPK14 in DFG-out mode and exhibits an IC_{50} of 4 nM, and inhibits other p38 isoforms, but at much lower potencies (IC_{50} = 520 nM for MAPK13) [32]. Superposition of BIRB- 796 into MAPK13 indicated it could sterically clash with the gatekeeper residue, so we designed inhibitors with smaller substituents at this position that we hypothesized would bind in DFG-out mode [20]. We began by determining the IC_{50} values in a steady-state enzyme inhibition assay. These values for 1-(3-tert-butyl-1-methyl-1H-pryzol-5-yl)-3-[4-(pyridin-4-yloxy)phenyl]urea (compound 61) and 2- (morpholin-4-yl)-N-[4-pyridin-4-yloxy)phenyl]pyridine-4-carboxamide (compound 124) were reported previously [20]. Here we determine the IC_{50} values for 1-(3-tert-butyl-1-methyl-1H-pyrazol-5- yl)-3-[4-(pyridin-4-ylsulfanyl)phenyl]urea (compound 58) and 3-(4-methyl-1H-imidazol-1-yl)-N-[4- (pyridin-4-xyloxy) phenyl] benzamide (compound 117) (Fig. 1a). Surprisingly, the IC_{50} values varied over a wide range; while compounds 58 and 61 displayed IC_{50} values in the nanomolar range, compounds 117 and 124 displayed IC_{50} values in the micromolar range, over 800-fold less potent (Figs. 1b and 1c).

3.2. Kinetic and binding analysis of inhibitors with MAPK13

Inhibitor binding kinetics has become an important drug design criteria. In particular, slow dissociation rates have been associated with improved inhibitor activities due to prolonged target engagement *in vivo* [33]. To understand whether inhibitor binding kinetics correlated with potency, we analyzed this property using biolayer interferometry (BLI), in a manner similar to that for compounds 61 and 124 reported previously [20]. In these assays, biotinylated MAPK13 was immobilized on the streptavidin- coated BLI pin and association

and dissociation kinetics were analyzed. The two compounds that displayed IC_{50} values in the nanomolar range displayed slower association and dissociation rates with around 100-fold longer complex half-lives ($t_{1/2}$ = 111 to 137 sec) as compared to inhibitor compounds with micromolar IC_{50} values ($t_{1/2}$ = 1 to 3 sec) (Fig. 2 a-c). These kinetic constants are of similar magnitude as those for MAPK14 complexes with inhibitors measured by surface plasmon resonance (SPR) [34]. We hypothesized that this difference could correlate with different binding modes or binding pockets utilized by the inhibitors.

3.3. MAPK13 inhibitors display two different binding modes

In order to elucidate how our novel inhibitors bound to MAPK13, we determined the X-ray crystal structures of the complexes (Table 1). We had noticed during our structural analysis of the inactive (MAPK13) and dually-phosphorylated active (MAPK13/pTpY) forms of the protein [22] that a significant portion of the activation loop (residues 173-180), which is ordered in the dual- phosphorylated protein, is not visible in our high resolution electron density maps of the unphosphorylated form. We therefore reasoned that we should be able to obtain inhibitor complexes with MAPK13 via soaking inhibitors into crystals of the unphosphorylated form, and indeed we were able to demonstrate the validity of this method previously with the crystal structures of MAPK13 in complex with compounds 61 (PDB ID: 4EYJ) and 124 (4EYM). We observed a strong difference electron density for the two new compounds using this method (Fig. 3c & e). We found that the compounds displaying nanomolar IC_{50} values all bound similarly and occupied the ATP binding pocket, as well as an adjacent pocket usually occupied by Phe169 (of the DFG motif), displacing it from this pocket (Fig. 3a, c-d, and Table 2). This mode of binding has been termed as “DFG-out” and was first observed in the complexes of c-Abl with Gleevac [35] and MAPK14 with BIRB-796 [36]. In contrast, compounds displaying micromolar IC_{50} values bound in a similar manner, but did not displace Phe169 from the pocket (Fig. 3b,e,f), binding to MAPK13 in what is known as “DFG-in” mode (Table 2). Thus, in the case of the MAPK13 inhibitors presented here, it appears that binding mode creates a marked difference in potency. However, it should be noted that highly potent inhibitors that bind to MAPK14 in DFG-in mode have been identified (e.g, skepinone-L [5] and SB203580 [37]), so binding mode does not always dictate efficacy.

3.4. Analysis of binding pocket interactions of inhibitors in complex with MAPK13

To understand the structural basis for the observed binding modes exhibited by the different MAPK13- inhibitor complexes, we performed a comprehensive analysis of the binding pockets occupied by each inhibitor. The inhibitors analyzed here have similar designs, consisting of a heterocyclic ring that interacts with the hinge region of MAPK13, a central aromatic that occupies the ATP-binding site, and a bulky (mostly hydrophobic) group, with these units spanned with by various polar linkers (Fig. 1a). The binding pockets were very similar, with similar numbers of van Der Waals contacts and hydrogen bonds to MAPK13. We found that, compared to the micromolar inhibitors, the nanomolar inhibitors engaged in one additional hydrogen bond with MAPK13 (3 versus 4) (Fig. 4c). All inhibitors engaged in hydrogen bonds with the backbone amide nitrogens of Met110 (in the hinge) and Asp168 (in the DFG motif) (Fig. 4a,b,d,e). The main difference was seen in interactions involving the side-chain carboxylic acid of Glu72. This side-chain engages in a hydrogen bond with

the linker between central aromatic and bulky hydrophobic groups in these inhibitors. The nanomolar inhibitors all contain urea linkers whereas the micromolar inhibitors both contain amide linkers. The second hydrogen bond made possible with the urea linkages (red arrow, Fig. 4a,b) assists to lock the bulky hydrophobic groups in relative conformations that require the moieties to bind to the Phe pocket, thus making these inhibitors selective for the DFG-out conformation of the kinase. In addition, the extra atom in the urea versus amide linkage likely assists in optimal positioning of terminal hydrophobic groups to access the allosteric Phe169 pocket. Analysis of the hinge hydrogen bond with the pyridine moieties found in each of these inhibitors showed that in the DFG-in inhibitors (compounds 58 and 61) this hydrogen bond is about 2.5 Å (Fig. 4f, h), whereas this distance is about 3.0 Å in the DFG-out inhibitors (117 and 124) (Fig. 4g, h). Thus it appears that the shorter linkage (amide versus urea) also impacts inhibitor potency by lowering the strength of the hinge hydrogen bond interaction in an attempt to optimally bind the hydrophobic pockets on the opposite end of the molecule. Therefore, it appears from analysis of these compounds in complex with MAPK13 that not only does the urea linkage provide additional hydrogen bonding ability with MAPK13, it also assists in providing optimal spacing of large ring groups to optimally bind to respective pockets, including the allosteric Phe169 pocket. However, it should be noted that biphenyl amide inhibitors similar to compounds 117 and 124 have previously been observed to bind to both DFG-in and DFG-out conformations of MAPK14 and bind in similar modes to those observed in our MAPK13 structures [34], thus the inclusion of such groups does not dictate that these inhibitors can only bind in DFG-in modes.

3.5. Sequence comparison of inhibitor binding pockets in mammalian MAPK13 proteins

Given that numerous animal systems are used for *in vitro* studies, we carried out analysis of MAPK13 sequences from higher mammals to examine whether there were any gross differences in the MAPK13 binding pockets for the inhibitors characterized here. The MAPK13 sequences for the species analyzed here averaged greater than 90% identity (Fig. 5). Of the numerous residues lining the binding pocket for the inhibitors, only one displayed a very conservative variation. Residue Phe109 (in the hinge region) is a Tyr in chicken MAPK13 (Fig. 5). Structure-based analysis of the inhibitor binding pocket sequence conservation would suggest that the inhibitors analyzed here should bind similarly to MAPK13 proteins in common animal models.

3.6. Thermodynamic stability of MAPK13 complexes with inhibitors

Previous studies have demonstrated the use of differential scanning fluorimetry as a method for identifying potential kinase inhibitors based on the enhanced thermal stability upon complexation [38, 39]. A general observation has been that more potent kinase inhibitors lend greater thermal stability to the protein [40]. We decided to analyze our diverse potency inhibitors using this method. We carried out experiments with both the inactive (unphosphorylated) MAPK13 and active (dually- phosphorylated) MAPK13/pTpY, as well as with MAPK14. First, we carried out a titration on MAPK13 to establish a dynamic range for the inhibitors (Fig. 6). Based on this result, we carried out subsequent experiments with 25 μM inhibitor. The differences in melting temperatures using the two forms of MAPK13 were similar, indicating that the inhibitors effectively bound both forms of the protein (Table

3). The melting point shifts were about a degree higher for MAPK13/pTpY, likely due to the fact that this form is stabilized by contacts involving the phosphorylated activation loop, [22] which would be dislodged by the DFG-out inhibitors. We found that the micromolar inhibitors (compounds 117 and 124) induced small increases in melting temperatures of MAPK13 (1-2° C). In contrast, the nanomolar inhibitors all induced large shifts in melting temperatures of MAPK13 (7-8° C). In addition, we found that our inhibitors induced larger T_m shifts in MAPK13 than MAPK14 (by a difference of 2-3 °C). For comparison, we also ran the DSF experiments with the potent MAPK14 inhibitor BIRB-796, which is optimized for MAPK14 (IC_{50} [MAPK14] = 4 nM; IC_{50} [MAPK13] = 520 nM) [32]. We found that the melting point shifts corresponded with the known differences in potencies (DTm [MAPK14] = 13.7 °C; [MAPK13] = 5.9 °C). Taken together, these results suggest our best inhibitors characterized here display slight selectivity for MAPK13 versus MAPK14, which should improve with optimization. Thus, the inhibitors which displayed the greatest potency and longest complex half-lives induced the greatest shift in thermal stability, indicating that this could be a robust screening method to presage inhibitor potency for MAPK13, and selectivity versus MAPK14.

3.7. Computational analysis of inhibitor complexes

We carried out computational docking studies to gain further insight into why subsets of inhibitors bind to the DFG-in conformation versus the DFG-out conformation of MAPK13. In these calculations, the inhibitors were introduced as SMILES strings (with no predefined conformation) and were flexible during docking. The inhibitors were docked to MAPK13 coordinates in both the DFG-in and DFG-out mode. For compounds 58 and 61, which bind in the DFG-out mode, the calculations reproduced the crystal structures extremely accurately when docked to the MAPK13 DFG-out coordinates (Table 4). However, they showed high variation and poor docking scores when docked to MAPK13 in DFG-in coordinates. In contrast, for compounds 117 and 124, which bind in DFG-in mode, the calculations accurately reproduced the crystal structure coordinates for the inhibitors regardless of whether MAPK13 was in DFG-in or DFG-out mode (Table 4). In other words, regardless of whether or not the Phe pocket was available for inhibitor moiety binding, the DFG-in inhibitors preferred to bind to the same pockets as observed in the crystal structure. These calculations indicate that this set of inhibitor structures can be predicted fairly accurately using GLIDE, and imply that part of the selective driving force is goodness of fit to the available pockets and the inherent structure preferred by inhibitor. To analyze this further, we carried out the same calculation using MAPK14 in both DFG-in and DFG-out mode as the receptor for these inhibitors. With the MAPK14 structures, we obtained similar results as with MAPK13, and the simulations reproduced inhibitors binding configurations observed in the MAPK13 co-crystal structures. Thus, regardless of the receiver kinase, the inhibitors take on configurations observed in the crystal structures, indicating that the major driving forces for this set of inhibitors is chemically-encoded structural constraints of the compound and shape complementarity to available pockets.

4. Conclusions

Here we present the functional, biophysical, and structural characterization of two new inhibitor complexes with MAPK13, as well as the first comprehensive functional, biophysical, and structural analysis of all four of our inhibitor complexes, including the first use of thermodynamic and computational methods to study these complexes. These represent the only four MAPK13 inhibitor complexes structurally characterized to date, and are thus extremely valuable to drug design efforts that target this emerging molecular target. The inhibitors examined here displayed widely varying potencies, with IC_{50} values in either the nanomolar range, or, greater than 800-fold less potent, in the micromolar range. These potencies correlated well with small-molecule binding kinetics measured by BLI. The nanomolar-potency inhibitors displayed complex half-lives about 100 times longer than those of the micromolar inhibitors. It should be noted that the half-lives measured here using BLI are comparable to those of MAPK14-inhibitor interactions measured by the comparable flow-based method of SPR [34]. Co-crystal structures of MAPK13 in complex with each of the four inhibitors revealed that the high potency inhibitors all bound to the kinase in DFG-out configuration, whereas the lower potency inhibitors both bound in DFG-in configuration. This is worth noting, since high potency inhibitors can be developed for either mode, for example skepinone-L [5] and SB203580 [37] are highly potent MAPK14 inhibitors that bind in DFG-in mode. Slow inhibitor dissociation rates have emerged as an important parameter for sustained efficacy of kinase inhibitors. In general, slower kinetics have been observed for inhibitors binding to the DFG-out mode of kinases, possibly due to kinetic constraints caused by the necessary structural reconfiguration [36, 41]. However, the structural mechanisms that influence inhibitor binding kinetics are poorly understood, thus comprehensive structural and kinetic studies such as those presented here are quite valuable in creating these correlations. It can be noted that the structures for the inhibitor complexes were derived by soaking inhibitors into already formed crystals, and thus, may not be reflective of solution structure. However, given the correlation between the solid state observation of binding modes and the solution state biophysical data (binding thermodynamics, kinetics, and IC_{50} values) and computational predictions, we believe this is highly unlikely.

Detailed analysis of the binding pockets for the inhibitors revealed that all inhibitors, regardless of potency, interacted with MAPK13 in a very similar fashion, forming hydrogen bonds with the same residues in all four structures. The high potency inhibitors all engaged in one additional hydrogen bond, but computational docking and chemical reasoning indicate that this is mostly driven by the preferred lowest energy configuration of the inhibitor, which is intrinsic to its structure, and the goodness of fit of that conformation to the available pockets. It is worth noting that one of the development points of the GLIDE software has been to predict accurate kinase complexes with inhibitors [42]. The complexes with MAPK13 characterized here were readily predicted and suggest that this software approach could be used effectively for *in silico* screening to identify new chemical families with the potential to bind MAPK13.

DSF has been shown previously to be an effective method for screening for potential binders and inhibitors of kinases, and the thermal melting shifts usually correlate well with affinity

[40]. We found this to be the case with the set of inhibitors here, with the thermal shifts also correlating with binding mode (DFG-in versus DFG-out). These thermal shifts appear to correlate with binding affinities of the inhibitors, as observed in our titration experiments. These experiments do suggest, however, that this method could be utilized effectively to identify new inhibitors for MAPK13 by screening and to prioritize ranking based on magnitude of melting point stabilization. These experiments also suggest this method could be used to screen for inhibitors that selectively target MAPK13 versus MAPK14. The inhibitors analyzed here have not been optimized yet for potency or selectivity, yet they do display some preference for binding MAPK13 in our DSF experiments. Combining our structural studies of inhibitor binding done here with sequence comparison of MAP13 versus MAPK14 [22], the most sequence divergent area that contacts the inhibitors is in the hinge region, thus this will be focus of our future iterations of inhibitor design.

Recent studies of disease models in MAPK13 knockout mice and cellular studies have highlighted the importance that signaling pathways relying on MAPK13 may contribute to several diseases, including certain types of asthma, arthritis, cancer, and diabetes [15, 17-20]. Altogether, the functional, structural, and biophysical characterizations presented here provide the first comprehensive analysis of this type for inhibitor complexes with MAPK13, elucidating the structural basis for their mechanism of action, thus providing a knowledge base for the structure-based development of potent, and eventually specific, inhibitors.

Acknowledgements

This work was supported in part by funding from NIH R01-HL119813 (T.J.B), CADET P50- HL107183, CADET II UH2-HL123429 (M.J.H.), American Heart Association Predoctoral Fellowships PRE19970008 (Z.Y.) and PRE22110004 (D.L.K.), and a pre-doctoral training grant T32- GM007067 (D.L.K.). Results were derived from work performed at Argonne National Laboratory (ANL) Structural Biology Center and the Advanced Light Source, Berkeley CA (ALS). ANL is operated by U. Chicago Argonne, LLC, for the U.S. DOE, Office Biological and Environmental Research (DE-AC02-06CH11357). ALS is supported by the Office of Basic Energy Sciences of the U.S. DOE (DE-AC02-05CH11231).

References

[1]. Feng YJ, Li YY. The role of p38 mitogen-activated protein kinase in the pathogenesis of inflammatory bowel disease. J Dig Dis. 2011; 12:327–332. [PubMed: 21955425]

[2]. Schieven GL. The p38alpha kinase plays a central role in inflammation. Curr Top Med Chem. 2009; 9:1038–1048. [PubMed: 19747121]

[3]. Muller S, Knapp S. Targeting kinases for the treatment of inflammatory diseases. Expert Opin Drug Discov. 2010; 5:867–881. [PubMed: 22823261]

[4]. Schnieders MJ, Kaoud TS, Yan C, Dalby KN, Ren P. Computational insights for the discovery of non-ATP competitive inhibitors of MAP kinases. Curr Pharm Des. 2012; 18:1173–1185. [PubMed: 22316156]

[5]. Koeberle SC, Romir J, Fischer S, Koeberle A, Schattel V, Albrecht W, Grutter C, Werz O, Rauh D, Stehle T, Laufer SA. Skepinone-L is a selective p38 mitogen-activated protein kinase inhibitor. Nat Chem Biol. 2012; 8:141–143. [PubMed: 22198732]

[6]. Azevedo R, van Zeeland M, Raaijmakers H, Kazemier B, de Vlieg J, Oubrie A. X-ray structure of p38alpha bound to TAK-715: comparison with three classic inhibitors. Acta Crystallogr D Biol Crystallogr. 2012; 68:1041–1050. [PubMed: 22868770]

[7]. Millan DS, Bunnage ME, Burrows JL, Butcher KJ, Dodd PG, Evans TJ, Fairman DA, Hughes SJ, Kilty IC, Lemaitre A, Lewthwaite RA, Mahnke A, Mathias JP, Philip J, Smith RT, Stefaniak MH,

Yeadon M, Phillips C. Design and synthesis of inhaled p38 inhibitors for the treatment of chronic obstructive pulmonary disease. J Med Chem. 2011; 54:7797–7814. [PubMed: 21888439]

[8]. Adams RH, Porras A, Alonso G, Jones M, Vintersten K, Panelli S, Valladares A, Perez L, Klein R, Nebreda AR. Essential role of p38alpha MAP kinase in placental but not embryonic cardiovascular development. Mol Cell. 2000; 6:109–116. [PubMed: 10949032]

[9]. Mudgett JS, Ding J, Guh-Siesel L, Chartrain NA, Yang L, Gopal S, Shen MM. Essential role for p38alpha mitogen-activated protein kinase in placental angiogenesis. Proc Natl Acad Sci U S A. 2000; 97:10454–10459. [PubMed: 10973481]

[10]. Tamura K, Sudo T, Senftleben U, Dadak AM, Johnson R, Karin M. Requirement for p38alpha in erythropoietin expression: a role for stress kinases in erythropoiesis. Cell. 2000; 102:221–231. [PubMed: 10943842]

[11]. Goldstein DM, Gabriel T. Pathway to the clinic: inhibition of P38 MAP kinase. A review of ten chemotypes selected for development. Curr Top Med Chem. 2005; 5:1017–1029. [PubMed: 16178744]

[12]. Risco A, del Fresno C, Mambol A, Alsina-Beauchamp D, MacKenzie KF, Yang HT, Barber DF, Morcelle C, Arthur JS, Ley SC, Ardavin C, Cuenda A. p38gamma and p38delta kinases regulate the Toll-like receptor 4 (TLR4)- induced cytokine production by controlling ERK1/2 protein kinase pathway activation. Proc Natl Acad Sci U S A. 2012; 109:11200–11205. [PubMed: 22733747]

[13]. Risco A, Cuenda A. New Insights into the p38gamma and p38delta MAPK Pathways. J Signal Transduct. 2012; 2012:520289. [PubMed: 22175015]

[14]. O'Callaghan C, Fanning LJ, Barry OP. p38delta MAPK: Emerging Roles of a Neglected Isoform. Int J Cell Biol. 2014; 2014:272689. [PubMed: 25313309]

[15]. Sumara G, Formentini I, Collins S, Sumara I, Windak R, Bodenmiller B, Ramracheya R, Caille D, Jiang H, Platt KA, Meda P, Aebersold R, Rorsman P, Ricci R. Regulation of PKD by the MAPK p38delta in insulin secretion and glucose homeostasis. Cell. 2009; 136:235–248. [PubMed: 19135240]

[16]. Ittner A, Block H, Reichel CA, Varjosalo M, Gehart H, Sumara G, Gstaiger M, Krombach F, Zarbock A, Ricci R. Regulation of PTEN activity by p38delta-PKD1 signaling in neutrophils confers inflammatory responses in the lung. J Exp Med. 2012; 209:2229–2246. [PubMed: 23129748]

[17]. Del Reino P, Alsina-Beauchamp D, Escos A, Cerezo-Guisado MI, Risco A, Aparicio N, Zur R, Fernandez- Estevez M, Collantes E, Montans J, Cuenda A. Pro-oncogenic role of alternative p38 mitogen-activated protein kinases p38gamma and p38delta, linking inflammation and cancer in colitis-associated colon cancer. Cancer Res. 2014

[18]. Zur R, Garcia-Ibanez L, Nunez-Buiza A, Aparicio N, Liappas G, Escos A, Risco A, Page A, Saiz-Ladera C, Alsina-Beauchamp D, Montans J, Paramio JM, Cuenda A. Combined deletion of p38gamma and p38delta reduces skin inflammation and protects from carcinogenesis. Oncotarget. 2015; 6:12920–12935. [PubMed: 26079427]

[19]. Criado G, Risco A, Alsina-Beauchamp D, Perez-Lorenzo MJ, Escos A, Cuenda A. Alternative p38 MAPKs are essential for collagen-induced arthritis. Arthritis Rheumatol. 2014; 66:1208–1217. [PubMed: 24782184]

[20]. Alevy YG, Patel AC, Romero AG, Patel DA, Tucker J, Roswit WT, Miller CA, Heier RF, Byers DE, Brett TJ, Holtzman MJ. IL-13-induced airway mucus production is attenuated by MAPK13 inhibition. J Clin Invest. 2012; 122:4555–4568. [PubMed: 23187130]

[21]. Lee MR, Dominguez C. MAP kinase p38 inhibitors: clinical results and an intimate look at their interactions with p38alpha protein. Curr Med Chem. 2005; 12:2979–2994. [PubMed: 16378500]

[22]. Yurtsever Z, Scheaffer SM, Romero AG, Holtzman MJ, Brett TJ. The crystal structure of phosphorylated MAPK13 reveals common structural features and differences in p38 MAPK family activation. Acta Crystallogr D Biol Crystallogr. 2015; 71:790–799. [PubMed: 25849390]

[23]. Otwinowski Z, Minor W. Processing of X-ray diffraction data collected in oscillation mode. Methods in Enzymology. 1997; 276:307–326.

[24]. Emsley P, Cowtan K. Coot: model-building tools for molecular graphics. Acta Crystallogr D Biol Crystallogr. 2004; 60:2126–2132. [PubMed: 15572765]

[25]. Adams PD, Grosse-Kunstleve RW, Hung LW, Ioerger TR, McCoy AJ, Moriarty NW, Read RJ, Sacchettini JC, Sauter NK, Terwilliger TC. PHENIX: building new software for automated crystallographic structure determination. Acta Crystallogr D Biol Crystallogr. 2002; 58:1948–1954. [PubMed: 12393927]

[26]. Laskowski RA, Swindells MB. LigPlot+: multiple ligand-protein interaction diagrams for drug discovery. J Chem Inf Model. 2011; 51:2778–2786. [PubMed: 21919503]

[27]. Schrodinger, LLC. The PyMOL Molecular Graphics System. Version 1.3r1. 2010 in.

[28]. Morin A, Eisenbraun B, Key J, Sanschagrin PC, Timony MA, Ottaviano M, Sliz P. Collaboration gets the most out of software. Elife. 2013; 2:e01456. [PubMed: 24040512]

[29]. Meyer PA, Socias S, Key J, Ransey E, Tjon EC, Buschiazzo A, Lei M, Botka C, Withrow J, Neau D, Rajashankar K, Anderson KS, Baxter RH, Blacklow SC, Boggon TJ, Bonvin AM, Borek D, Brett TJ, Caflisch A, Chang CI, Chazin WJ, Corbett KD, Cosgrove MS, Crosson S, Dhe-Paganon S, Di Cera E, Drennan CL, Eck MJ, Eichman BF, Fan QR, Ferre-D'Amare AR, Christopher Fromme J, Garcia KC, Gaudet R, Gong P, Harrison SC, Heldwein EE, Jia Z, Keenan RJ, Kruse AC, Kvansakul M, McLellan JS, Modis Y, Nam Y, Otwinowski Z, Pai EF, Pereira PJ, Petosa C, Raman CS, Rapoport TA, Roll-Mecak A, Rosen MK, Rudenko G, Schlessinger J, Schwartz TU, Shamoo Y, Sondermann H, Tao YJ, Tolia NH, Tsodikov OV, Westover KD, Wu H, Foster I, Fraser JS, Maia FR, Gonen T, Kirchhausen T, Diederichs K, Crosas M, Sliz P. Data publication with the structural biology data grid supports live analysis. Nat Commun. 2016; 7:10882. [PubMed: 26947396]

[30]. Halgren TA, Murphy RB, Friesner RA, Beard HS, Frye LL, Pollard WT, Banks JL. Glide: a new approach for rapid, accurate docking and scoring. 2. Enrichment factors in database screening. J Med Chem. 2004; 47:1750–1759. [PubMed: 15027866]

[31]. Friesner RA, Banks JL, Murphy RB, Halgren TA, Klicic JJ, Mainz DT, Repasky MP, Knoll EH, Shelley M, Perry JK, Shaw DE, Francis P, Shenkin PS. Glide: a new approach for rapid, accurate docking and scoring. 1. Method and assessment of docking accuracy. J Med Chem. 2004; 47:1739–1749. [PubMed: 15027865]

[32]. Kuma Y, Sabio G, Bain J, Shpiro N, Marquez R, Cuenda A. BIRB796 inhibits all p38 MAPK isoforms in vitro and in vivo. J Biol Chem. 2005; 280:19472–19479. [PubMed: 15755732]

[33]. Wood ER, Truesdale AT, McDonald OB, Yuan D, Hassell A, Dickerson SH, Ellis B, Pennisi C, Horne E, Lackey K, Alligood KJ, Rusnak DW, Gilmer TM, Shewchuk L. A unique structure for epidermal growth factor receptor bound to GW572016 (Lapatinib): relationships among protein conformation, inhibitor off-rate, and receptor activity in tumor cells. Cancer Res. 2004; 64:6652–6659. [PubMed: 15374980]

[34]. Angell RM, Angell TD, Bamborough P, Bamford MJ, Chung CW, Cockerill SG, Flack SS, Jones KL, Laine DI, Longstaff T, Ludbrook S, Pearson R, Smith KJ, Smee PA, Somers DO, Walker AL. Biphenyl amide p38 kinase inhibitors 4: DFG-in and DFG-out binding modes. Bioorg Med Chem Lett. 2008; 18:4433–4437. [PubMed: 18602262]

[35]. Schindler T, Bornmann W, Pellicena P, Miller WT, Clarkson B, Kuriyan J. Structural mechanism for STI-571 inhibition of abelson tyrosine kinase. Science. 2000; 289:1938–1942. [PubMed: 10988075]

[36]. Pargellis C, Tong L, Churchill L, Cirillo PF, Gilmore T, Graham AG, Grob PM, Hickey ER, Moss N, Pav S, Regan J. Inhibition of p38 MAP kinase by utilizing a novel allosteric binding site. Nat Struct Biol. 2002; 9:268–272. [PubMed: 11896401]

[37]. Wang Z, Canagarajah BJ, Boehm JC, Kassisa S, Cobb MH, Young PR, Abdel-Meguid S, Adams JL, Goldsmith EJ. Structural basis of inhibitor selectivity in MAP kinases. Structure. 1998; 6:1117–1128. [PubMed: 9753691]

[38]. Niesen FH, Berglund H, Vedadi M. The use of differential scanning fluorimetry to detect ligand interactions that promote protein stability. Nat Protoc. 2007; 2:2212–2221. [PubMed: 17853878]

[39]. Vedadi M, Niesen FH, Allali-Hassani A, Fedorov OY, Finerty PJ Jr. Wasney GA, Yeung R, Arrowsmith C, Ball LJ, Berglund H, Hui R, Marsden BD, Nordlund P, Sundstrom M, Weigelt J, Edwards AM. Chemical screening methods to identify ligands that promote protein stability, protein crystallization, and structure determination. Proc Natl Acad Sci U S A. 2006; 103:15835–15840. [PubMed: 17035505]

[40]. Fedorov O, Niesen FH, Knapp S. Kinase inhibitor selectivity profiling using differential scanning fluorimetry. Methods Mol Biol. 2012; 795:109–118. [PubMed: 21960218]

[41]. Gruenbaum LM, Schwartz R, Woska JR Jr. DeLeon RP, Peet GW, Warren TC, Capolino A, Mara L, Morelock MM, Shrutkowski A, Jones JW, Pargellis CA. Inhibition of pro-inflammatory cytokine production by the dual p38/JNK2 inhibitor BIRB796 correlates with the inhibition of p38 signaling. Biochem Pharmacol. 2009; 77:422–432. [PubMed: 19027720]

[42]. Lyne PD, Lamb ML, Saeh JC. Accurate prediction of the relative potencies of members of a series of kinase inhibitors using molecular docking and MM-GBSA scoring. J Med Chem. 2006; 49:4805–4808. [PubMed: 16884290]

[43]. Gouet P, Robert X, Courcelle E. ESPript/ENDscript: Extracting and rendering sequence and 3D information from atomic structures of proteins. Nucleic Acids Res. 2003; 31:3320–3323. [PubMed: 12824317]

Highlights

- First comprehensive analysis of MAPK13/inhibitor complexes of widely varied potency
- Inhibitors of nanomolar IC_{50} bind in DFG-out mode; micromolar IC_{50} bind DFG-in
- Nanomolar IC_{50} correlates with longer dissociation half-lives
- Binding thermodynamics of inhibitors correlates with potency
- The data provide a guide for designing high potency inhibitors to MAPK13

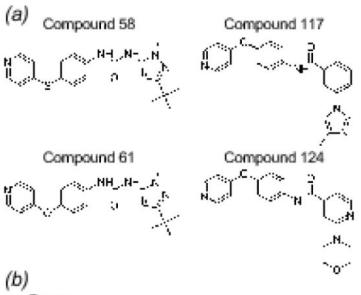

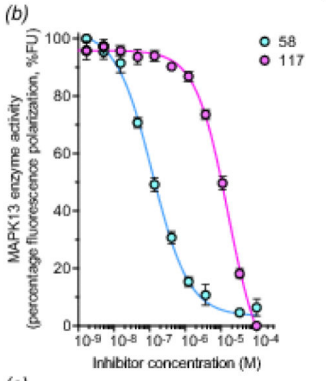

(c)

Compound	IC_{50}(nM)	95% Confidence	R^2
58	117	87-165	0.99
61*	620	530-724	0.99
117	15785	12530-19885	0.99
124*	98747	28862-337855	0.90

Figure 1.

Schematic of MAPK13 inhibitors and their IC_{50} values. *(a)* Schematic of MAPK13 inhibitor compounds characterized in this manuscript. *(b)* Data and curve fit used to determine IC_{50} values for compounds 58 and 117. Values represent mean and error bars are SEM. *(c)* IC_{50} values, 95% confidence range, and coefficients of determination (R^2). * denotes values were previously reported [20].

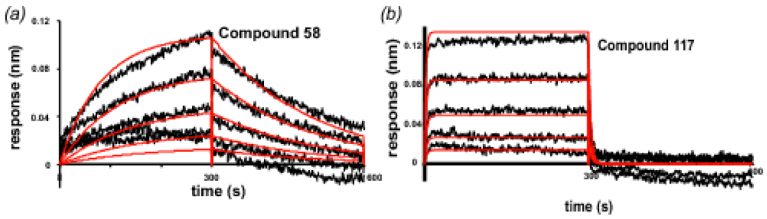

(c)

Compound	$t_{1/2}$(sec)	Binding Mode
58	137	DFG-out
61*	111	DFG-out
117	3	DFG-in
124*	1	DFG-in

Figure 2.

Biolayer interferometry analysis of MAPK13 binding to inhibitors. *(a-b)* Biolayer interferometry sensorgrams for *(a)* compound 58 and *(b)* compound 117. Processed data are shown as black lines with global kinetic fits overlaid as red lines. *(c)* Table of MAPK13-inhibitor complex half-lives derived from the global kinetic fits of $k_{association}$ and $k_{dissociation}$ ($t_{1/2} = \ln 2/k_{dissociation}$). * denotes values were previously reported [20].

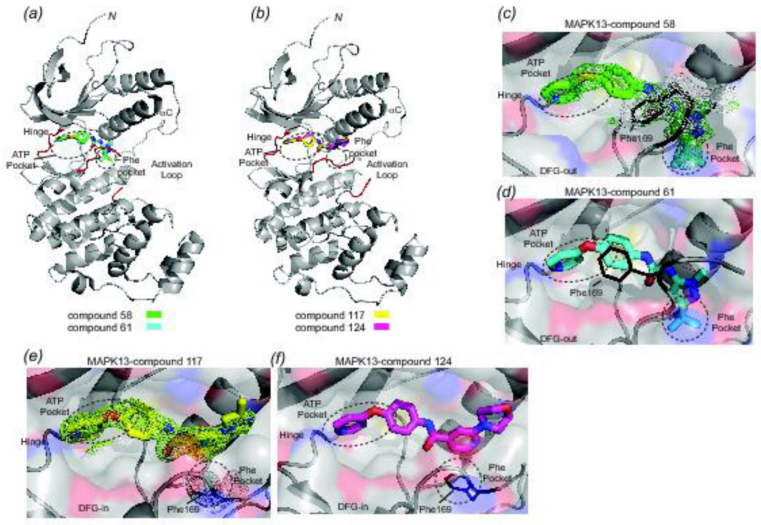

Figure 3.

Structures of MAPK13 complexes with inhibitors. *(a)* Ribbon diagram of MAPK13 (grey) with DFG-out inhibitors 58 and 61. Hinge and activation loop are both colored red. *(b)* Ribbon diagram of MAPK13 (grey) with DFG-in inhibitors 117 and 124. Hinge and activation loop are both colored red. *(c)* Crystal structure of compound 58 (green) in complex with MAPK13 in DFG-out mode. Omit *Fo – Fc* electron density contoured at 3.0 σ is shown for the compound and *2Fo – Fc* electron density contoured at 2.0 σ is shown for Phe169. *(d)* Our previously reported crystal structure of compound 61 (cyan) in complex with MAPK13 in DFG-out mode for comparison (4EYJ). *(e)* Crystal structure of compound 117 (yellow) in complex with MAPK13 in DFG-in mode. Omit *Fo – Fc* electron density contoured at 3.0 σ is shown for the compound and *2Fo – Fc* electron density contoured at 2.0 σ is shown for Phe169. *(f)* Our previously reported crystal structure of compound 124 (magenta) in complex with MAPK13 in DFG-in mode for comparison (4EYM). The dynamic positioning of Phe169 of the DFG motif is shown in all complexes.

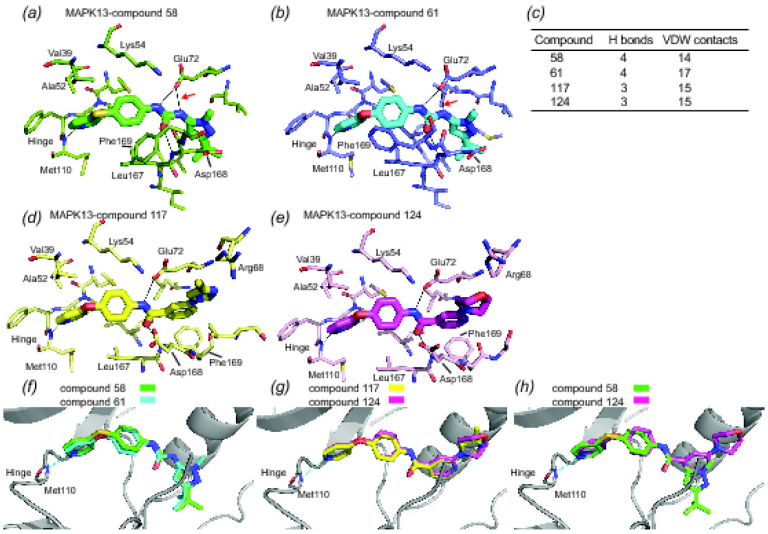

Figure 4.

MAPK13 binding pockets for inhibitor compounds. Binding pockets for *(a)* compound 58, *(b)* compound 61, *(d)* compound 117, and *(e)* compound 124. All residues that make van der Waals or polar contacts are shown. Hydrogen bonds are shown as thin black lines. One hydrogen bond that is unique to compounds 58 and 61 as compared to 117 and 124 is highlighted with the red arrow. *(c)* Table of polar and non-polar contacts each compound makes with MAPK13. *(f-h)* Overlay comparison showing hinge interactions with the pyridinyl rings of *(f)* compounds 58 and 61, *(g)* compounds 117 and 124, and *(h)* compounds 58 and 124. Note in *(h)* that there is a displacement of 0.5Å for the pyridinyl nitrogen in comparing 58 and 124.

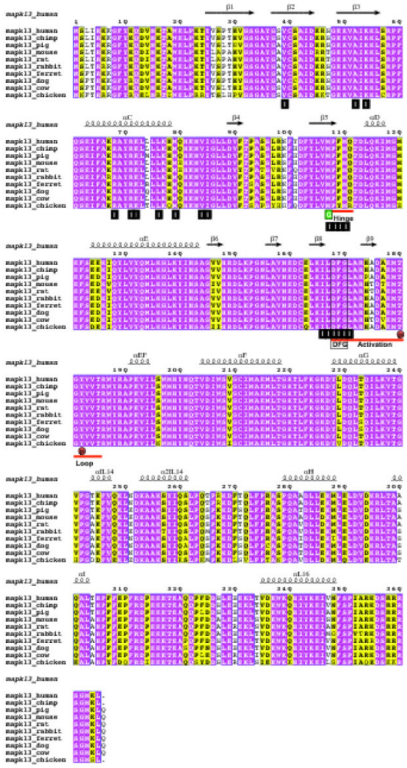

Figure 5.

Sequence alignment of MAPK13 from relevant disease model mammals. Invariant and conserved residues are highlighted with magenta and yellow backgrounds, respectively. Secondary structure of human MAPK13 is shown above the alignment. The hinge region, DFG motif, gatekeeper (G), dual phosphorylation site (P), and activation loop are shown. Residues that form the binding pockets for inhibitor compounds are marked (black I). Figure was generated using *ESPript3.0* [43].

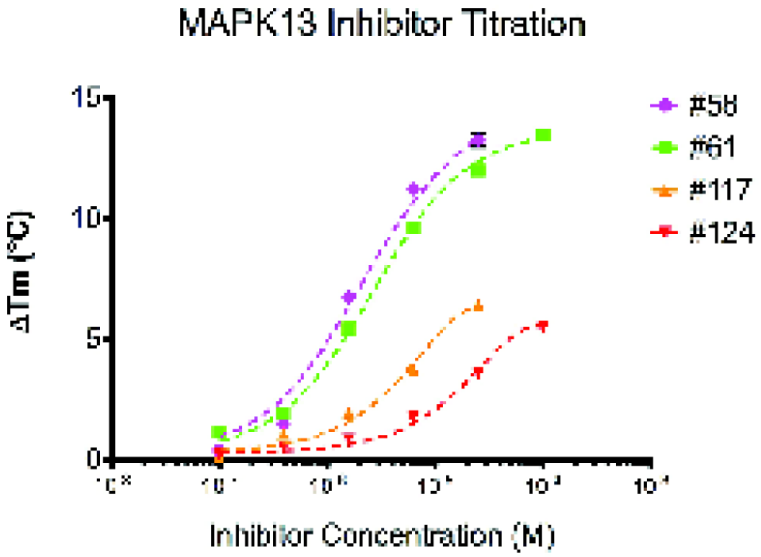

Figure 6.

Changes in MAPK13 melting temperatures (ΔT_m) induced by binding inhibitors as measured by DSF. Titration of inhibitors is shown while MAPK13 concentration was held at 0.15 mg/ml. The point at each concentration is an average of three replicate experiments conducted with different protein preps.. Error bars are SEM. Curve fitting done in PRISM 5 using the one site total binding equation for nonlinear regression. Calculated Kd's listed in Table 3.

Table 1

Crystallographic statistics for MAPK13 complexes with inhibitor compounds

Compound	58	117
Data collection statistics		
Space Group	$P2_12_12_1$	$P2_12_12_1$
Unit Cell (Å)	a=61.0 b=70.2 c=92.9	a=61.3 b=69.7 c=93.1
Source	ALS 4.2.2	APS 19-ID
Wavelength(Å)	1.0000	0.9790
Resolution(Å)	50.0-2.60 (2.69−)	50.0-2.00 (2.07−)
R_{sym}(%)	9.1 (50.8)	5.5 (36.9)
Completeness(%)	88.5 (100)	81.2(87.8)
Redundancy	7.0(7.3)	4.6(4.4)
I/σ(I)	20.6(3.6)	21.6(2.5)
Refinement statistics		
R_{work} (%)	21.8	20.0
R_{free} (%)	27.3	24.1
Amino Acid Residues(#)	340	340
Waters (#)	23	213
RMSD bond length (Å)/angles(°)	0.003/0.667	0.004/0.904
Wilson B ($Å^2$)	48.4	31.3
Ave B. protein	52.2	37.0
Ave. B inhibitor	40.5	31.3
Ave. B water	48.1	42.7
Ramachandran		
%Favored	87.4	95.3
%Allowed	12.0	4.4
%Outliers	0.6	0.3
Poor rotamers (no. / %)	12 / 3.99%	5 / 1.6%
Clashscore (score / percentile)	6.72 / 99^{th}	6.10 / 95^{th}
Molprobity (score / percentile)	2.16 / 94^{th}	1.83 / 85^{th}
Luzzati Error	0.35	0.24
PDB ID	5EKN	5EKO

Values in parenthesis are for the highest-resolution shell.

Table 2

Backbone torsion angles that define the conformation of the MAPK13 DFG motif

		Leu 167		Asp 168		Phe 169	
Compound	**DFG conformation**	**φ(°)**	**Ψ(°)**	**φ(°)**	**Ψ(°)**	**φ(°)**	**Ψ(°)**
58	DFG-out	−124.5	170.8	−154.0	150.4		
61	DFG-out	−119.6	169.4	−144.7	93.6	−66.0	−22.9
117	DFG-in	−107.8	156.4	62.5	37.1	−82.5	150.0
124	DFG-in	−111.3	160.9	55.5	39.7	−81.9	162.6

Table 3

Inhibitor-induced thermal stability shifts measured by differential scanning fluorimetry (DSF)

Compound	AT_m-MAPK13 (°C)*	AT_m-MAPK13/pTpY (°C)*	AT_m-MAPK14 (°C)*	Kd (μM)**
58	8.1 ± 0.3	9.0 ± 0.4	5.2 ± 0.3	1.9 ± 0.3
61	7.2 ± 0.3	7.8 ± 0.4	5.1 ± 0.3	2.6 ± 0.5
117	1.8 ± 0.4	2.0 ± 0.5	−1.4± 0.4	N.D. ***
124	1.1 ± 0.3	1.2 ± 0.5	−0.8± 0.3	N.D
BIRB-796	5.9± 0.2		13.7± 0.3.	

* T_m are reported at inhibitor concentrations of 25 μM and kinase concentrations at 2.5 μM

** Derived from titrations shown in Fig. 6

*** Not determined

Table 4

GLIDE *in silico* docking results compared to co-crystal structures

Compound	58		61		117		124	
	Score*	RMSD**	Score	RMSD	Score	RMSD	Score	RMSD
MAPK13 DFG-out	−9.91	1.26	−8.88	1.23	−8.85	1.42	−8.24	1.62
MAPK13 DFG-in	−5.34	10.15	−5.21	9.99	−9.81	1.07	−6.14	2.00
MAPK14 DFG-out	−9.25	1.34	−8.70	1.10	−7.96	1.92	−4.20	12.71
MAPK14 DFG-in	−4.10	11.92	−4.16	12.25	−5.26	9.71	−8.15	3.57

*Glide Score in kcal/mol

**RMSD of compound heavy atom positions compared to crystal structure (Å)